Experimental study on the full cycle evolution of high-intensity atmospheric dc arc discharge from breakdown to extinguishment

Ya-Hao Hu,[1,2] Su-Rong Sun [1,*] Xian Meng [2] He-Ji Huang [2] and Hai-Xing Wang [1,3,†]

[1]*School of Astronautics, Beihang University, Beijing 100191, Beijing, China*
[2]*Institute of Mechanics, Chinese Academy of Sciences, Beijing 100190, Beijing, China*
[3]*Ningbo Institute of Technology, Beihang University, Ningbo 315800, Ningbo, China*

In this study, the spatiotemporal evolution of full cycle of high-intensity dc argon arc discharge at atmospheric pressure is investigated by using a transferred arc device, which is easy to be directly observed in the experiment. Combining the voltage and current waveforms with high-speed images, the full cycle evolution process of high-intensity atmospheric dc arc can be divided into five different stages: breakdown pulse stage, cathode heating stage, current climbing stage, stable arc discharge stage, and finally arc extinguishing stage. The characteristics of each different stage are analyzed in detail through the electrical properties, high-speed pictures, and spectroscopic measurements. The results show that the strong luminescence region develops from the vicinity of cathode and anode to the middle in the breakdown pulse stage, which is explained from the spatiotemporal evolution of distributions of excited argon atom and ions. The development velocity of emission intensity of argon ions is mainly determined by the dominant stepwise ionization process. Then the cathode heating stage appears with many bright and nonuniformly distributed light spots on the cathode surface, and the electron emission mechanism of cathode gradually changes to the thermionic emission as the surface temperature rises. With the increase of arc current, the discharge channel significantly expands, then becomes stable due to the increment of the Lorentz force. The characteristics of arc extinguishing stage are clarified in terms of the decay of charged particles density.

I. INTRODUCTION

The full cycle process of high-intensity atmospheric direct current (dc) arc plasma is very complicated, which may include the breakdown process between the electrodes, the establishment and development process of the arc discharge channel, the stable arc discharge stage, and so on [1]. Many researchers have focused on the study of arc plasma characteristics in the stable discharge stage, since this stage is easy to be investigated by experimental measurements [2–4] and numerical modeling [5–7]. However, to-date, there is no literature on the entire life cycle of arc plasma evolution process, thus, in this way our knowledge on high-intensity dc arc plasma is not comprehensive. Therefore, it is necessary to perform a detailed study on the full cycle process of arc plasma in order to find the interesting physical phenomena and realize better applications in the field of materials processing [8–10], aerospace propulsion [11–13], waste treatment [14–16], and so on.

Although the novel thermal and chemical nonequilibrium model coupling with space charge sheath has been developed to study the arc plasma characteristics [17–19], it is still very difficult to establish a unified numerical model on simulating the whole formation process of high-intensity dc arc, since the development of arc evolution process involves many different

stages. Conducting experimental research can better observe the arc full cycle process, and is much closer to the real situation of arc plasma formation.

The present experimental study on atmospheric arc plasma mainly focuses on the electrical properties [20–22], arc temperature measurement [23–25], and anode heat flux [26–28]. These studies improve our understanding on the arc plasma, but only on the stable discharge stage after the arc formation. The development of arc formation is a dynamic process, which requires both the temporal and spatial measurement to capture the entire process. There are a few measurements on spatiotemporal evolution of breakdown process in an atmospheric discharge [29–31]. Parkevich *et al.* [32] used multiframe laser probing system to find that the atmospheric air breakdown is related with the fast formation ($\leqslant 1$ ns) of a micron-sized cathode spot with an electron density of about 10^{19} cm^{-3}, which can be transformed into a spark channel having an electron density of 10^{19}–10^{20} cm^{-3}.

Besides the stable arc discharge stage and fast breakdown, the formation of high-intensity atmospheric pressure dc arc discharge also involves other abundant physical phenomena, such as the rise of cathode temperature, the change of electrons emission mechanism and the establishment of arc discharge channel with the increment of arc current. Although some numerical researches on cathode heating and cathode spot mode of atmospheric pressure arc have been performed [33–37], the experimental study on the cathode spot evolution characteristics of atmospheric arc discharge is very scarce. Phan *et al.* [38] performed experimental observation of
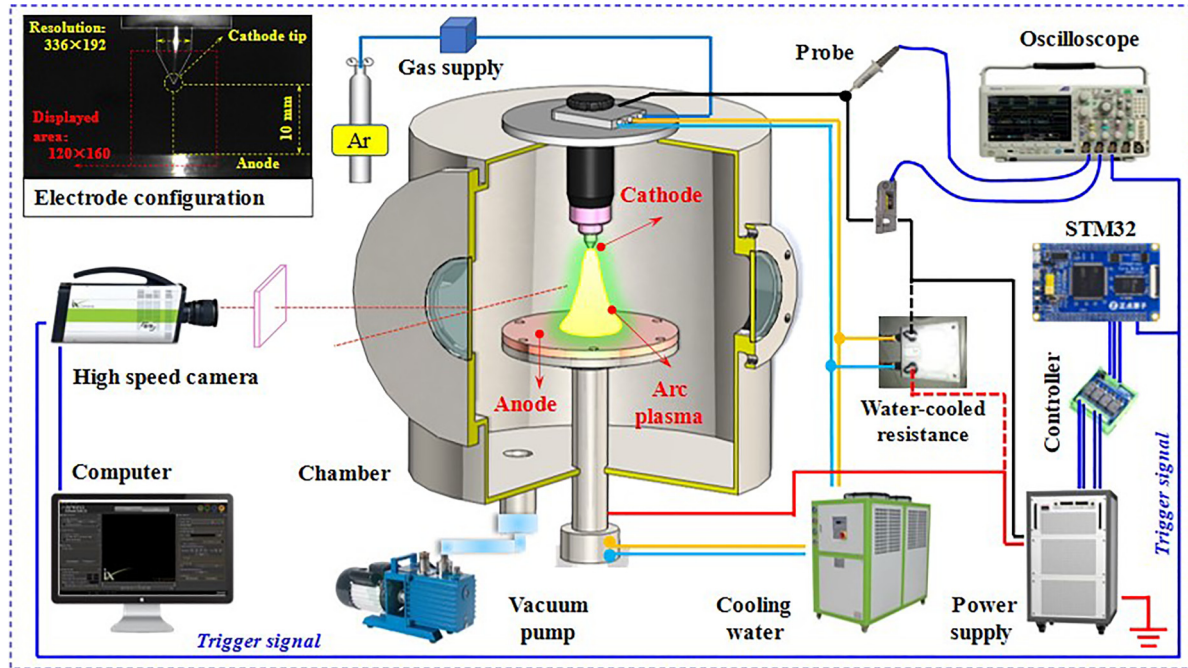
*ssr18@buaa.edu.cn
†whx@buaa.edu.cn

FIG. 1. Schematic of the experimental setup.

cathode spot behavior in argon alternating current tungsten inert gas welding of aluminum by using high-speed video camera, illustrating the general tendency of the life cycle of the cathode spot. It is found the cathode spots exhibit an uneven and ring-shaped distribution, and have a random movement on the surface. Schein *et al.* [39] investigated the ignition of arc spots on cold cathode in a pure argon gas atmosphere by electrical measurements and high-speed photography, and an initiation by a diffuse glow discharge and a constricted arc spot was observed, which were attributed to different surface structures. However, the detailed information about cathode spot behavior is still lack during the entire life cycle of high-intensity atmospheric dc arc.

It can be seen from the above analysis that there are basically corresponding studies on different arc discharge stage. However, these different discharge stages are investigated separately, actually they are related to each other, so it is more appropriate to investigate the entire life cycle process of high-intensity dc arc discharge, including the establishment and development process of the arc discharge channel and the arc extinguishing stage. In our experiment, a transferred arc device, shown in Fig. 1, is used to facilitate direct observation. The high-speed camera combined with the spectroscopic diagnostic are adopted to observe the temporal and spatial evolution of the high-intensity atmospheric dc arc discharge. The details about the experimental setup are given in Sec. II. In Sec. III, we first present the full spatiotemporal evolution cycle of the arc discharge, which involves the breakdown pulse stage, the cathode heating stage, the current climbing stage, the stable arc discharge and eventually the arc extinguishing stage when turning off the power supply. Then the mechanisms for each discharge stage are clarified in order to better comprehend the phenomena associated with different discharge stages. Finally, the conclusion is given in Sec. IV.

II. EXPERIMENTAL SETUP

Figure 1 shows the schematic of the experimental system used in this study, mainly including a core chamber, a transferred arc device, a power supply, a water cooler, a vacuum pump, and the measurement and control system. The transferred arc device is placed in the core chamber with a diameter of 600 mm and a height of 550 mm as shown in Fig. 1. The high-intensity dc arc discharge is generated between a thoriated tungsten cathode with the diameter of 5 mm and a copper anode, which are cooled by water. The detailed electrode configuration is exhibited in the upper left corner of Fig. 1. The conical cathode with a 60° cone angle is perpendicular to anode surface, and the electrodes gap is fixed as 10 mm. An insulated-gate bipolar transistor inverter dc constant-current power supply with the current adjustment range of 40–160 A is used, and the arc current is set to 85 A in this study. However, the open-circuit voltage of the power supply is ∼430 V, which is not enough to cause breakdown. Therefore, an independent discharge circuit, which can generate the high-voltage pulse of 10 kV with the width of ∼6 μs and the frequency of ∼80 Hz, is equipped in the power supply to create breakdown. Once there is breakdown between the electrodes, the independent discharge circuit stops working immediately. Before the experiment, the air in the chamber is pumped out by the vacuum pump, then the argon working gas with the purity of 99.999% is used to flush the chamber, finally the argon working gas is refilled to the chamber until reaching one atmosphere. The water-cooled resistance of 0.1 Ω is used to test the power supply, and replaced by the arc discharge when the experiment begins.

The voltage and current signals of the arc discharge are respectively collected by a high-voltage probe (Tektronix P6015A) and a current probe (Cybertek CP8150A) together with a digital oscilloscope (Tektronix MDO3034). The
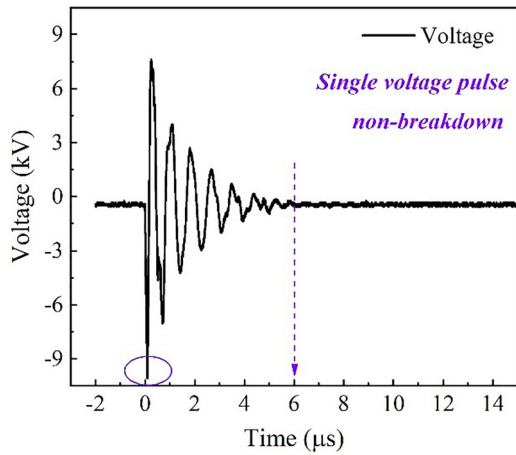
FIG. 2. The waveform of the high-voltage pulse.

sampling rate of the oscilloscope is set to 5M Sa/s. Figure 2 shows the waveform of the high-voltage pulse collected by the high-voltage probe. It can be seen that the peak value of breakdown voltage is about 10 kV. The variation range of voltage during the whole discharge process is very large ($10 \sim 10^4$ V), such as, $\sim$10 kV of breakdown voltage, $\sim$430 V of open-circuit voltage and $\sim$15 V of stable argon arc discharge voltage. Therefore, in order to clearly see the voltage change in the whole discharge cycle, it is necessary to select an appropriate scale for the oscilloscope measurement range.

In our paper the selected measurement scale is from -550 to 250 V, although some high voltage signals will be lost, the evolution process of the voltage after breakdown can be clearly exhibited.

A monochromatic high-speed camera (*i*-speed 513) is used to directly observe the spatiotemporal evolution of high-intensity arc discharge. The frame rate is set to 100 000 fps with an exposure time of 1 μs. The image taken by the high-speed camera before discharge is shown in upper left corner of Fig. 1. The resolution of the image is 336×192 pixels, and the area enclosed by a red dashed line with 120×160 pixels is selected to exhibit the arc discharge state in the Sec. III. A single chip microcomputer (STM32) is adopted to control the power supply and trigger the high-speed camera, which ensures that the discharge image sequence can be synchronized with the voltage and current waveforms for further analysis. The distributions of excited argon atoms and argon ions are respectively acquired by two narrowband filters at the central wavelengths of 696 and 375 nm, respectively, with a bandwidth of 10 nm.

III. EXPERIMENTAL RESULTS AND DISCUSSION

A. Spatiotemporal evolution of full cycle of high intensity dc arc

Figure 3 shows the spatiotemporal evolution of high intensity dc arc in an entire discharge cycle. According to the voltage and current waveforms collected by the oscilloscope
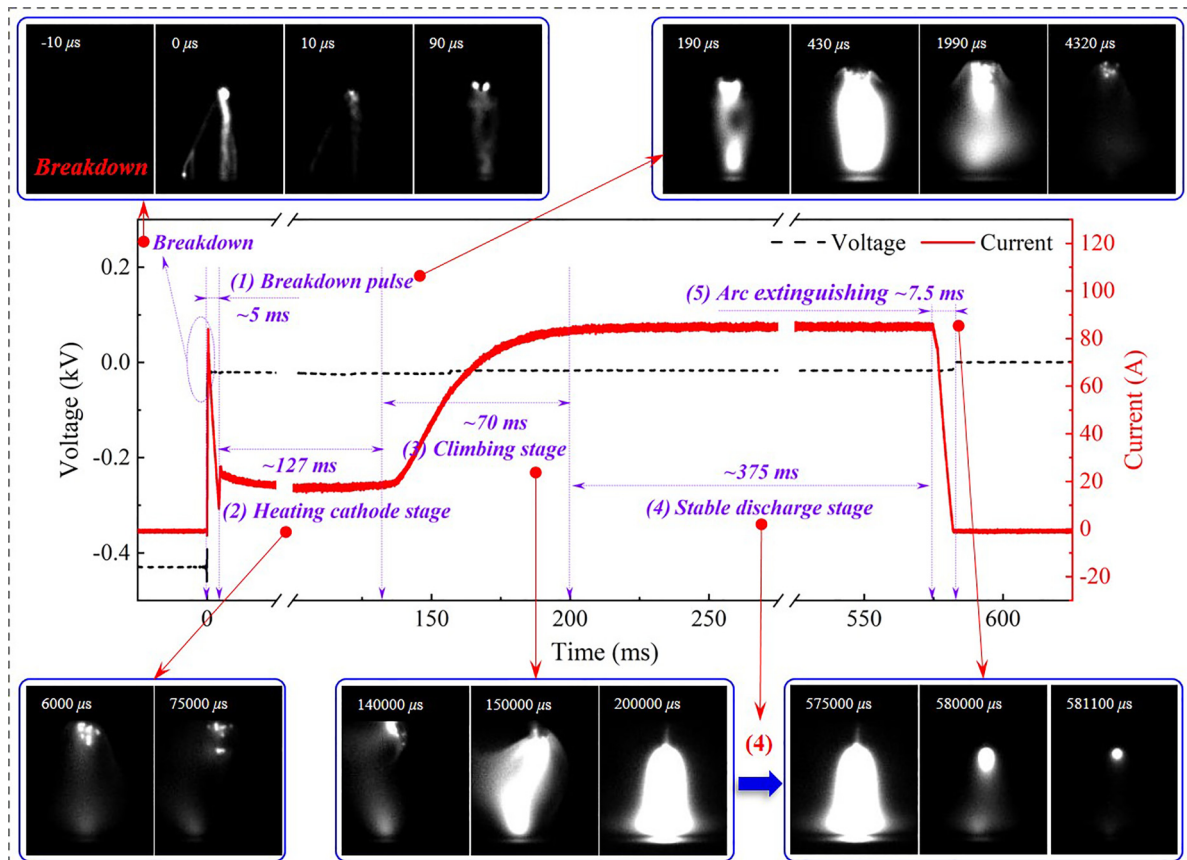

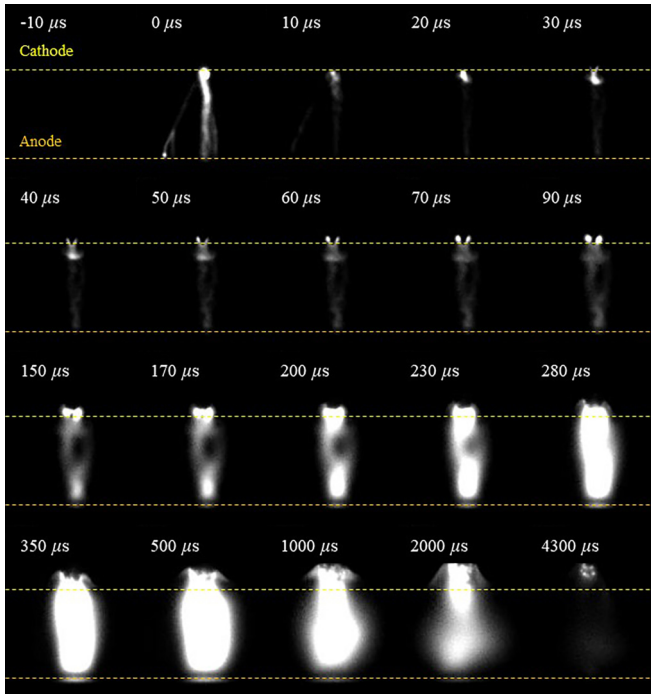FIG. 3. Spatiotemporal evolution of full cycle of high intensity dc arc.

FIG. 4. Evolution of the discharge channel in the breakdown pulse stage.

and the discharge images taken by the high-speed camera, the development process of high-intensity dc arc can be divided into five different stages, including the breakdown pulse stage, the cathode heating stage, the current climbing stage, the stable discharge stage, and the arc extinguishing stage. As shown in Fig. 3, the breakdown process between the electrodes is completed within 1 μs, which is too fast to capture the detail by the camera, and the breakdown discharge channel exhibits a multibranch structure. The breakdown pulse stage is characterized by a large current pulse lasting about 5 ms with a steep current rise time of 0.5 ms. Then the discharge enters a low current stage with a current value of about 20 A and a duration of ∼127 ms. In this stage the corresponding arc state is very unstable with many bright and irregularly moving spots on the cathode surface, which also heat the cathode. Therefore, this stage is defined as the cathode heating stage. After that,

the arc current gradually increases to the set value of 85 A, and the stable discharge channel of high-intensity dc arc is established. Then the arc enters the stable discharge stage, which is widely used and investigated for practical applications in thermal arc field. When the power supply is switched off, the arc extinguishing stage begins, in this stage the arc current drops rapidly in a short time, and the corresponding discharge channel also delays fast. Further detailed analyses and descriptions of each stage in the full development process of high-intensity dc arc are given below.

B. The breakdown pulse stage

Figure 4 exhibits the spatiotemporal evolution processes of the discharge channel in the breakdown pulse stage synchronized with the variations of voltage and current shown in Fig. 5. At the time $t = 0$ μs, the voltage peak value reaches about 10 kV (as shown in Fig. 2), leading to the strong electric field on the order of 10^6 V/m, however, this is an estimated average electric field based on the electrodes gap, considering the influence of the surface microscale structure, the field enhancement factor is in the range of 10–1000 [25,40], so the maximum local electric field could reach the order of 10^9 V/m. The work function of thoriated tungsten cathode used in the experiment is 2.6 eV, and the required electric field for cathode to emit electrons is on the order of 10^9 V/m. Therefore, this maximum local electric field in the experiment could extract free electrons from the thoriated tungsten cathode surface, then the emitted electrons can be accelerated by the high sheath voltage, inducing the ionization impact reactions, and forming a bright spark discharge channel with multibranch structure as shown in the high-speed image at the time of 0 μs in Fig. 4. In the process, the electrode temperature is relatively low and the thermionic emission can be ignored. Thus, the field emission is dominated in this stage.

After the time $t = 0$ μs, the voltage decreases rapidly and becomes positive close to 10 μs in Fig. 5(b), resulting in the fast drop of electric field and the reversal of electric field direction. Thus, the discharge channel cannot be maintained and decays fast at the time $t = 10$ μs since the energy obtained from the external electric field is reduced and the collision interactions between the free electrons and argon atoms are also weakened. Then the voltage returns to negative values
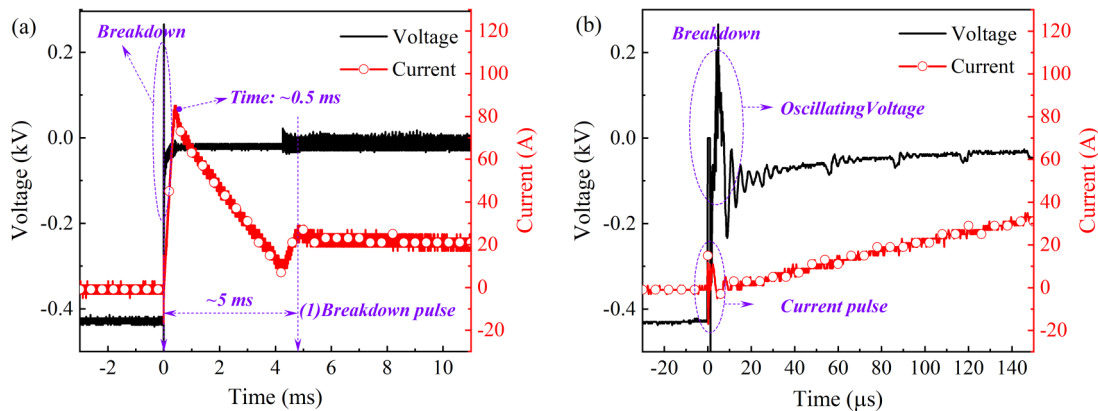

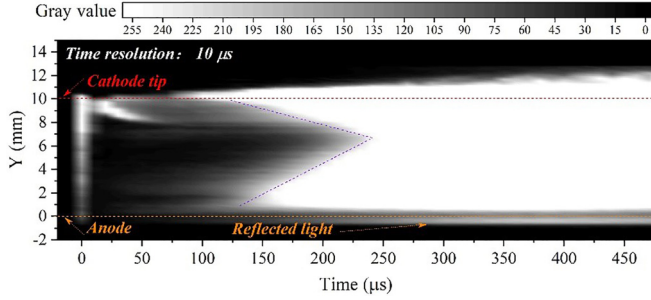FIG. 5. Voltage and current waveforms in the breakdown pulse stage.

FIG. 6. Spatiotemporal evolution process of the discharge channel.

and shows oscillation, so the energy is gradually accumulated during this pulse stage. Moreover, the direction of the electric field does not change after 10 μs, and the electric field gradually becomes stable. The electrons in the discharge channel can obtain energy from the electric field again, producing more excited species and charged particles, thus the discharge channel gradually develops, and the current rises at a rate of about 160 A/ms in the time range of 20–500 μs as seen from Fig. 5(a), in which the increase of the current is nearly linear, and the current is about 3 A at $t = 20$ μs and 80 A at $t = 500$ μs. Until the time of 150 μs, the cathode and anode luminescence are very strong, indicating that the discharge channel develops from the vicinity of the two electrodes to the middle as shown in the time sequences of 150–280 μs in Fig. 4.

In order to clearly see the evolution of the discharge channel, Fig. 6 shows the spatiotemporal evolution process of the discharge channel in the breakdown pulse stage obtained by imitating streak camera, where the Y axis is the space position between electrodes and the X axis is the time. From the front development of the strong light emission near the electrodes, the development speed of the discharge channel near the cathode and anode are estimated to be 28 m/s and 52 m/s, respectively. The current reaches the peak value at the time of 500 μs, the corresponding discharge channel area also reaches the maximum value, as shown in the high-speed image at $t = 500$ μs in Fig. 4. After that, the discharge attenuates again due to the decrease of discharge current.

Figure 7, respectively, presents the spatiotemporal evolution of the emission intensity of excited argon atoms and argon ions obtained with a narrowband filter at the central wavelengths of 696 nm and 375 nm with a bandwidth of 10 nm. Combining with the emission intensity of excited argon atoms and argon ions, the phenomenon of discharge channel developing from two electrodes vicinity to the middle can be explained. From Fig. 7(a), it is seen that the excited argon atoms mainly exist close to the cathode before the time of 100 μs, then it begins to develop near the anode, and fills the entire discharge gap between cathode and anode at the time of about 300 μs, which is consistent with the variations of discharge images taken by high-speed camera in Fig. 6.

However, the emission intensity of argon ions in Fig. 7(b) shows a development trend from cathode to anode. The distribution of argon ions is determined by the following equation:

$$\frac{\partial \rho_i}{\partial t} + \nabla \cdot \vec{J}_i + \nabla \cdot (\rho_i \vec{u}_g) = S_{c,i}. \qquad (1)$$
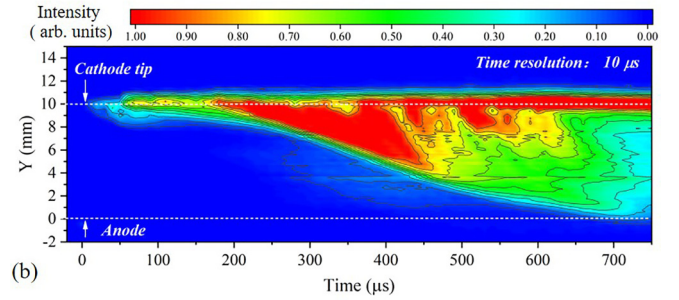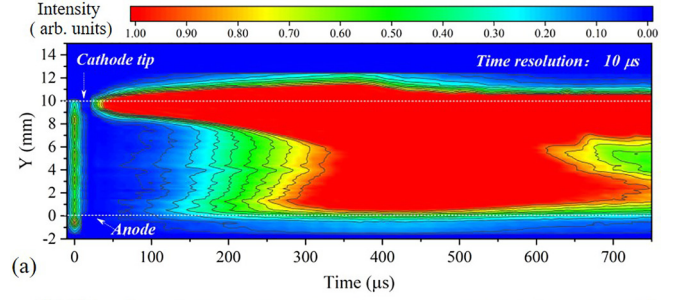

FIG. 7. Spatiotemporal evolution of the emission intensity of excited argon atoms and ions at the central wavelengths of 696 and 375 nm, respectively, in the breakdown pulse stage.

The second term and the third term on the left-hand side, respectively, describe the diffusion and convective effects on ions density, $S_{c,i}$ is the chemical reactions source term. At the time scale of about 100 μs, the diffusion and convective processes play a small role on the argon ions development, and the chemical reactions processes are critical for the argon ions distribution. The ionization reactions mainly include the electron impact of ground state argon atoms, and excited argon atoms ionization by electron impact (namely, stepwise ionization),

$$e^- + \mathrm{Ar} \rightarrow 2e^- + \mathrm{Ar}^+, \qquad (2)$$

$$e^- + \mathrm{Ar}^* \rightarrow 2e^- + \mathrm{Ar}^+. \qquad (3)$$
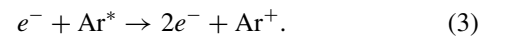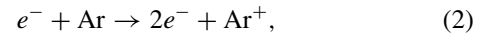
From Fig. 7, it can be seen that large emission intensity of argon ions occurs at the positions where the intensity of excited states of argon atoms is high. Therefore, the ionization of argon atoms is mainly through stepwise ionization, and the direct ionization caused by electron collision with argon ground state is relatively weak during the argon ions development. According to previous study [17,41], the cathode sheath voltage can account for about 40% of the total voltage, and the anode sheath voltage is negligible, so the electrons can obtain much more energy near the cathode, resulting in more intense ionization and the light emission of ions developing from the cathode to the anode. It is estimated from Fig. 7(b) that the development speed of the front of the ions emission intensity is about 21.27 m/s. The front development speed of argon ions emission intensity is mainly determined by the rate of ionization reactions in the breakdown pulse stage, since the effect of convection and diffusion processes on ions distribution is small. Based on the above analysis, the dominant ionization reaction is the step ionization with the rate coefficient $k = 1.37 \times 10^{-13} T_e[\mathrm{eV}]^{0.5} \exp(-4.11 / T_e[\mathrm{eV}])$ m^{3}s^{-1} [5]. The front development speed v of argon ions emission
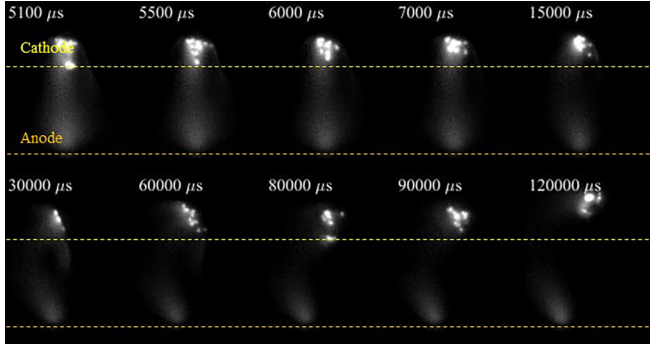
FIG. 8. Evolution of the discharge channel in the cathode heating stage.

intensity can be derived as follows:

$$v = \frac{dV}{A} = \frac{dN_e}{An_e} = \frac{n_e n_{Ar^*} kAL}{An_e} = n_{Ar^*} kL, \qquad (4)$$

where dV is the change rate of discharge volume, A is the area of discharge front, dN_e is the change rate of electrons number, n_e is the number density of electron behind the discharge front, n_{Ar^*} is the number density of excited argon atom, k is the rate coefficient of step ionization, and L is the length of the intense emission region behind the front. In Eq. (4), the electron temperature and excited states density are required to calculate the development velocity of ions emission intensity. In atmospheric argon arc discharges, the electron temperature is usually about 1–2 eV [1,24,42]. Below electron temperatures of 1 eV, the step ionization coefficient k is about 2.24×10^{-15} m^3/s [5], n_{Ar} is about 5.3×10^{23} m^{-3} based on the Saha equation in the thermodynamic equilibrium assumption, and n_{Ar^*} is about 5.3×10^{18} m^{-3} according to the Boltzmann relation. The emission length L is on the order of 10^{-3} m seen from the discharge image. Based on these data, the front development speed v can be estimated on the order of 10 m/s, which is consistent with the speed estimated from Fig. 7(b). Therefore, it is concluded that the development of ions distributions in this stage is mainly dominated by the electron impact excited state ionization process.

C. The cathode heating stage

At the end of the breakdown pulse stage, the discharge current decreases to about 20 A as shown in Fig. 3, so the discharge image has changed significantly, and the discharge mode enters the cathode heating stage. Figure 8 shows the image sequences of the discharge channel in this stage photographed by a high-speed camera, which has the exposure time of 1 μs. In this stage, there are many bright and nonuniformly distributed spots on the cathode surface, which also move irregularly. Compared with the cathode spots, the discharge column has a weak luminous intensity, and exhibits the distortion with the increase of time.

This cathode heating stage is characterized by low arc voltage of about 20 V, thus leading to the small electric field strength. Under the action of this weak electric field, the collision excitation and ionization interactions between different particles are reduced, causing the weak light emission of the discharge channel in Fig. 8. Similarly, the cathode surface

processes are also influenced by the weak electric field. The average electric field intensity is estimated on the order of 10^3 V/m, which is much less than the field intensity required for field emission $\sim 10^9$ V/m. Therefore, the field emission of the cathode is not enough to provide sufficient electrons, and the cathode electron emission mechanism must have changed in the cathode heating stage. It is pointed out in Ref. [43] that the secondary electron emission caused by the exited argon atoms and ions impact the cathode surface becomes the main emission process when the cathode is not heated enough to thermionic emission. The secondary electron emission coefficient caused by the impact of excited argon atoms on the cathode has been estimated to be of the order of 1 [44,45], while the secondary emission coefficient of positive ions is only about 0.1 [46], so it is considered that the secondary electron emission process due to the excited atoms impact is stronger than that caused by the impact of argon ions. Moreover, these excited argon atoms diffuse to cathode surface and loss the excited energy by radiation, leading to the bright luminescence near the cathode surface.

The ions from the plasma region can obtain energy from the cathode sheath, and bombard the cathode surface, generating a nonlinear heating of the cathode. As pointed out in Ref. [33], this nonlinear heating could cause the occurrence of cathode spots. The power balance of the cathode surface can be written as follows:

$$\frac{j_i}{e}\left(eU_{sh}^c + A_i - A_f\right) = \frac{j_{em}}{e}A_f + q, \qquad (5)$$

where j_i and j_{em} are respectively the ion current density and the electron emission current density, U_{sh}^c is the cathode sheath voltage drop, A_i is the ionization energy of argon, A_f is the work function of cathode material, and e is the elementary charge. This simple equation indicates that the ions heating for the cathode is balanced by the energy taken away by the emitted electrons leaving the cathode surface and the heat conduction. The detailed analysis of heat flux along the cathode surface has been given in our previous papers [41], which also shows that the space-sheath heating and ion recombination are the dominant heating mechanisms for the cathode, and the energy taken away by the emission electrons is the main heat dissipation process. The variation of heat flux with the surface temperature is nonmonotony, at relatively low T_w, the net energy flux to the cathode surface increases with the surface temperature, then this could cause a new increase in the cathode surface temperature, but when T_w is very large and the ionization degree on the plasma side approaches unity, the net energy flux decreases [33]. This phenomenon could inhibit the thermal instability and result in the final formation of stable arc-cathode attachment. Moreover, it can be seen from Fig. 8 that the bright spots on the cathode surface moves irregularly. The movement of these cathode spots may interfere with the flow field, which could be responsible for the distortion of the discharge channel. Finally, as the cathode surface temperature increases, the cathode gradually becomes hot with the obvious thermal radiation appearing on the surface, and the cathode electron emission is converted to the thermionic emission.

In order to better see the characteristics in cathode heating stage, Fig. 9 exhibits the image sequences of the cathode heating process at an electrode gap of 3 mm taken by a Sony
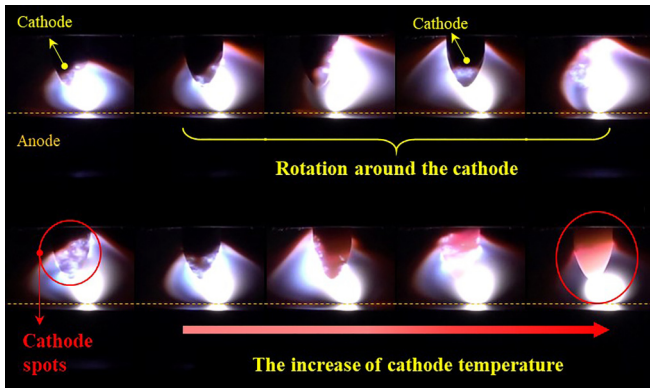
FIG. 9. Heating effect of cathode spots on cathode.

camera (FDR-AX700). The frame rate of the image sequences is 100 fps and the exposure time is 0.1 ms. From Fig. 9 it is seen that there are many unevenly distributed bright spots on the cathode surface, i.e., the cathode spots. Moreover, these bright spots show the rotation around the cathode surface, meanwhile the distortion of the arc discharge channel also can be clearly observed due to the rotation of the cathode spots. Then the cathode is gradually heated to a very high temperature and turns red as the time increases, exhibiting an intense thermal radiation characteristic. Finally, the cathode becomes a hot cathode, and the discharge is stabilized near the cathode tip.

D. The current climbing stage

Figure 10 exhibits the image sequences of the discharge channel in the current climbing stage synchronized with the variations of voltage and current shown in Fig. 3. In this stage, the discharge current gradually increases from about 20 A to the set value of 85 A, the cathode spots gradually disappear, and the discharge area on the cathode surface converges near the cathode tip, since the cathode tip temperature is high enough to ensure the thermionic emission after the heating stage, keeping the current continuity. With the increase of time, the distorted discharge channel becomes bell shape at the time of ∼160 ms, then the discharge channel expands radially to form a stable arc discharge. This is because the self-induced magnetic field becomes strong at large arc current, producing large Lorentz force to stabilize the discharge channel.
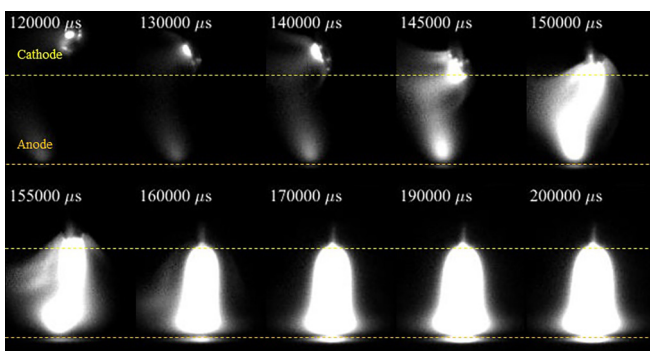

FIG. 10. Evolution of the discharge channel in the current climbing stage.
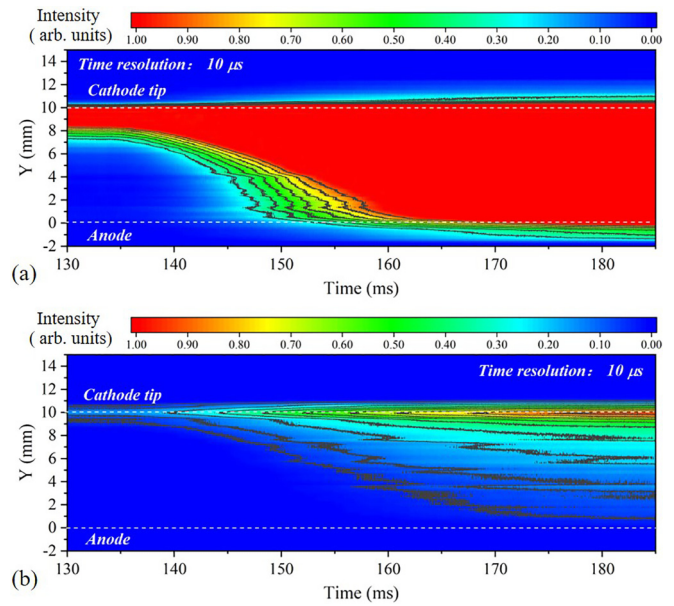

FIG. 11. Spatiotemporal evolution of the emission intensity of excited argon atoms (a) and ions (b) at the central wavelengths of 696 nm and 375 nm respectively in the current climbing stage.

Figure 11, respectively, shows the spatiotemporal evolution of the emission intensity of excited argon atoms and argon ions. Before $t = 140$ ms, the emission intensity of excited argon atom is very strong near the cathode region, which may correspond to the luminescence of cathode spots as explained in the cathode heating stage. Then, with the increase of arc current, the electron impact excitation process gradually becomes strong and develops in the entire discharge channel, thus the number density of excited argon atoms rises, causing the area with strong emission intensity reaching the anode.

In Fig. 11(b) the evolution trend of the emission intensity of argon ion is similar to that of the excited argon atom. However, the ionization rate is mainly controlled by the electron impact excited argon atom, so its development speed (∼0.24 m/s) from the cathode to anode is slower than that of the excited argon atom (∼0.36 m/s). The distributions of argon ions can still be described by Eq. (1), but different from the breakdown pulse stage, the time scale in the current climbing stage is large, so the effect of diffusion and convective processes on the distributions of argon ions should be considered. Moreover, from the arc images, it is observed that the discharge channel is almost axisymmetric in the breakdown pulse stage, while it is distorted during the current rise stage caused by the gas flow actions. Until the time of 170 ms, the discharge channel presents a stable bell shape. In arc discharge, the main force inducing the flow is the Lorentz force, and the magnitude of this force is closely related to the current density. At $t = 170$ ms, the arc current rises to about 85 A, and the discharge area on cathode surface is estimated about 0.78×10^{-6} m^2, hence, the current density increases to about 1.08×10^8 A/m^2, producing large Lorentz force. The enhanced cathode jet promotes the intense excitation and ionization region developing towards the anode and filling the entire electrodes gap.
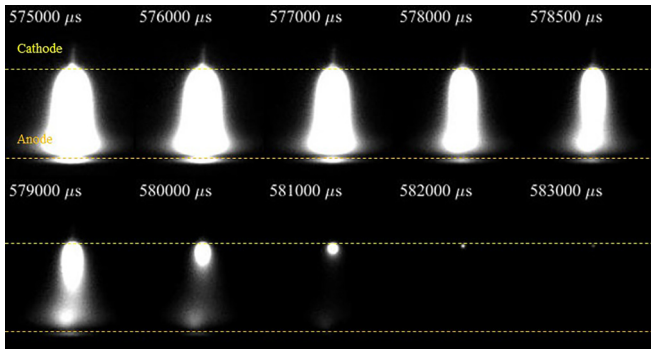
FIG. 12. Evolution of the discharge channel in the arc extinguishing stage.

FIG. 14. The correlation between discharge area and arc current.

E. The arc extinguishing stage

After the stable discharge stage of ~375 ms, the power supply is switched off, and the discharge enters the extinguishing stage with a rapid decrease of arc current from the fixed value of 85 A to 0 A. Figure 12 exhibits the evolution of the discharge channel in the arc extinguishing stage. It is seen that the discharge channel first contracts radially, then decays axially. In the time range of 575–577 ms, although there exists obvious radial contraction phenomenon, the discharge channel is still stable and symmetric. After that, with the further decrease of arc current, the constricted discharge channel becomes asymmetric near the anode due to the reduced cathode jet effect. The radial and axial decay processes of the discharge channel are better clarified in Fig. 13. As can be seen, the intense light emission region begins to move away from the anode surface after $t \approx 577$ ms, implying the start of asymmetrical constriction of the discharge channel near the anode. Then the discharge channel begins to exhibit
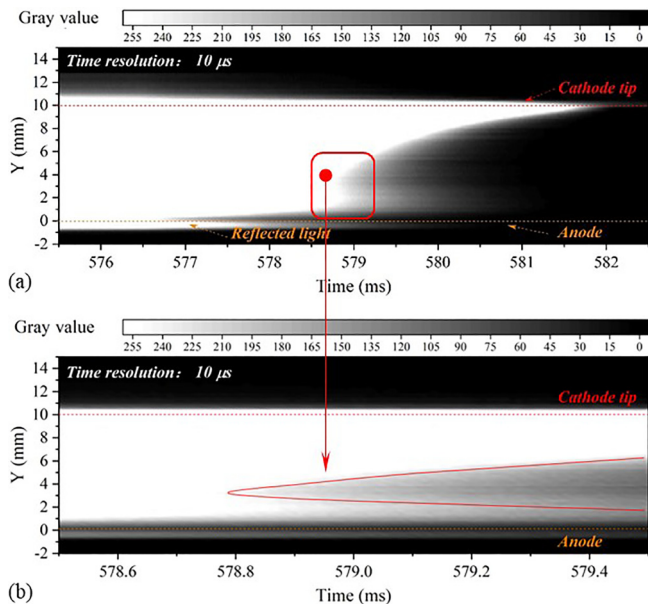

FIG. 13. Spatiotemporal evolution of the discharge channel in the arc extinguishing stage, (a) the entire arc extinguishing stage, (b) the partial enlarged view in red box.
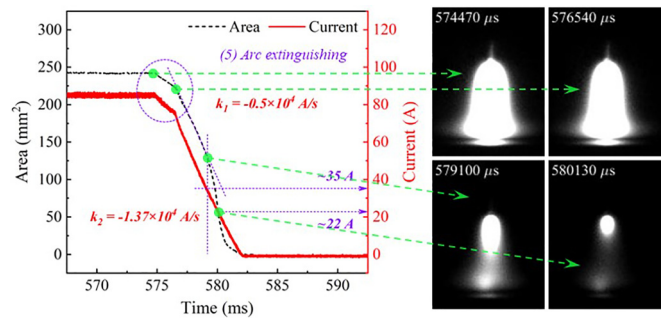
obvious axial decay from the arc column to the electrodes at $t \approx 578.8$ ms as shown in Fig. 13(b), in which the solid red line stands for the boundary of intense light emission region. Finally, the luminescence near the anode disappears completely after $t \approx 580$ ms, while the bright light near the cathode gradually disappears until the arc current decreases to 0 A at $t \approx 582$ ms. The cathode tip still can emit light due to the thermal radiation after the discharge channel disappears completely.

Figure 14 presents the correlation between discharge area and arc current in the arc extinguishing stage. The variation trend of discharge area and arc current shows good consistency. At $t = 574.5$ ms, the discharge area begins to decrease at a rate of ~10.2 mm^2/ms until the time of 576.5 ms, and the discharge image mainly shows the radial contraction. In this range the corresponding arc current has a slight decrease from 85 to 75 A. Then the discharge area experiences a fast drop from the time of 576.5 ms to 579.1 ms. Meanwhile, the discharge image not only shows the radial contraction, but also presents the axial decay. And the current drops to ~35 A at a rate of -1.37×10^4 A/s. As the arc current further declines, the decay rate of discharge area first increases then decreases. The image of the discharge channel only shows bright luminescence below the cathode due to the low current and the weak cathode jet. From this analysis, it is concluded that the variation of discharge images is almost determined by the decrease of arc current.

As pointed out in our previous paper [47,48], in the discharge decay stage, the electron temperature and electric field drop over a very short time, and the densities of charged and excited species are relatively low. So, in order to see the evolution of different species, Fig. 15, respectively, shows the spatiotemporal evolution of the emission intensity of excited argon atoms and argon ions. It can be seen that both the excited argon atoms and argon ions show the similar decay trend from the near anode region to the cathode, and the decay rate of argon ions is faster than that of excited argon atoms. This may be caused by the generation of excited argon atoms during the recombination process of argon ions, including the three-body recombination reaction and dissociative recombination reaction [5,6,49]. The recombination reactions of argon ions develop fast towards the cathode region, leading to the decrease of electron density. When the number density of charged particles in the discharge channel is too low to maintain the discharge, the arc is extinguished.
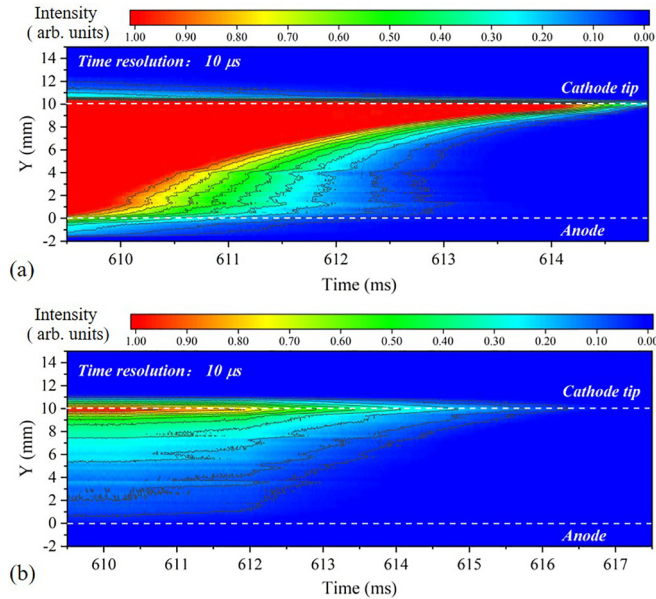
FIG. 15. Spatiotemporal evolution of the emission intensity of excited argon atoms (a) and ions (b) at the central wavelengths of 696 and 375 nm, respectively, in the arc extinguishing stage.

IV. CONCLUSION

In this paper, the experimental study has been carried out for a transferred arc device to investigate the spatiotemporal evolution of full cycle of high-intensity dc argon arc discharge. It is found that the entire cycle evolution process of high-intensity dc arc discharge can be divided into five different stages, i.e., breakdown pulse stage, cathode heating stage, current climbing stage, stable arc discharge stage and finally arc extinguishing stage. The time and space resolved arc discharge images obtained by high-speed camera are synchronized with the voltage and current waveforms to analyze the characteristics of each stage. Moreover, the distributions of excited argon atoms and argon ions are obtained with the narrowband filter to further clarify the evolution mechanism of the discharge channel under every different stage.

The experimental results show that the breakdown pulse stage is characterized by a large current pulse, in which the breakdown process occurs very quickly and is completed within 1 μs. After that, the discharge images present the corresponding behavior with the change of voltage and current waveforms. Up until the time of 150 μs, the luminescence near cathode and anode is very strong, indicating that the discharge channel develops from the vicinity of two electrodes to the middle, which is consistent with the spatiotemporal distribution of the excited argon atom. At the time of 500 μs

the current reaches the peak value, and the corresponding discharge area also achieves the maximum value. The spatiotemporal distribution of argon ions mainly develops from the cathode to anode. The development velocity of argon ions is calculated based on the dominant stepwise ionization reaction rate, which is the same order of magnitude as the measured grow rate of argon ions front.

In the cathode heating stage, there are many bright and nonuniformly distributed spots on the cathode surface, which also move irregularly. Due to the low arc voltage and electric field intensity, the cathode electron emission mechanism may evolve from the initial field emission to the secondary electron emission caused by the exited argon atoms and ions impact the cathode surface, which also gradually heat the cathode, and then to the thermionic emission with the rise of surface temperature. The excited argon atoms can diffuse to cathode surface and loss excited energy by radiation, leading to the bright and nonuniformly distributed light spots on the cathode surface. Finally, the cathode becomes hot, exhibiting an intense thermal radiation characteristic, and the discharge is stabilized near the cathode tip.

Then the discharge enters the current climbing stage. As the arc current increases, the discharge channel significantly expands and becomes the stable bell shape due to the increase of Lorentz force. In this stage, the distributions of excited argon atoms and ions are not only determined by the ionization reactions, but also affected by the convection and diffusion processes. Finally, when entering the arc extinguishing stage, the discharge channel first shows obvious radial contraction, and then presents both axial and radial decay. The variation of discharge images is closely related with the decline of arc current. Both the excited argon atoms and argon ions exhibit the similar decay trend from the near anode region to the cathode caused by the dominant de-excitation and recombination reactions with the decrease of arc current. The present results in this study are helpful to improve our understanding on the evolution mechanisms of full cycle process of high-intensity atmospheric dc arc discharge.

[1] A. B. Murphy and D. Uhrlandt, Foundations of high-pressure thermal plasmas, Plasma Sources Sci. Technol. **27**, 063001 (2018).

[2] R. M. Hartmann and J. V. R. Heberlein, Quantitative investigations on arc-anode attachments in transferred arcs, J. Phys. D **34**, 2972 (2001).

[3] G. Yang and J. V. R. Heberlein, Anode attachment modes and their formation in a high intensity argon arc, Plasma Sources Sci. Technol. **16**, 529 (2007).

[4] F. Liang, M. Tanaka, S. Choi, and T. Watanabe, Formation of different arc-anode attachment modes and their effect on temperature fluctuation for carbon nanomaterial

production in dc arc discharge, Carbon **117**, 100 (2017).

[5] M. Baeva, R. Kozakov, S. Gorchakov, and D. Uhrlandt, Two-temperature chemically nonequilibrium modelling of transferred arcs, Plasma Sources Sci. Technol. **21**, 055027 (2012).

[6] S. R. Sun, H. X. Wang, T. Zhu, and A. B. Murphy, Chemical nonequilibrium simulation of anode attachment of an argon transferred arc, Plasma Chem. Plasma Process. **40**, 261 (2020).

[7] C. Niu, Y. H. Hu, K. Shao, S. R. Sun, and H. X. Wang, Numerical simulation of the effect of annular boss structure on dc arc anode attachment, Plasma Chem. Plasma Process. **42**, 885 (2022).

[8] A. B. Murphy, A perspective on arc welding research: The importance of the arc, unresolved questions and future directions, Plasma Chem. Plasma Process. **35**, 471 (2015).

[9] S. Samal, Thermal plasma technology: The prospective future in material processing, J. Cleaner Prod. **142**, 3131 (2016).

[10] J. Xiang, H. Park, K. Tanaka, M. Shigeta, M. Tanaka, and A. B. Murphy, Numerical study of the effects and transport mechanisms of iron vapour in tungsten inert-gaswelding in argon, J. Phys. D **53**, 044004 (2020).

[11] C. J. Bersbach, J. Evans, H. Alkandry, M. E. Ewing, and D. A. Isaac, Ablative thermal response numerical modeling under arcjet test conditions, J. Thermophys. Heat Transfer **36**, 1 (2022).

[12] Y. M. Wei, Q. S. He, and H. X. Wang, Chemical nonequilibrium modeling of low-power nitrogen-hydrogen arcjet thrusters, J. Propul. Power **32**, 1 (2016).

[13] M. Nations, L. S. Chang, J. B. Jeffries, R. K. Hanson, M. E. MacDonald, A. Nawaz, J. S. Taunk, T. Gökçen, and G. Raiche, Characterization of a large-scale arcjet facility using tunable diode laser absorption spectroscopy, AIAA J. **55**, 1 (2017).

[14] J. V. R. Heberlein and A. B. Murphy, Thermal plasma waste treatment, J. Phys. D **41**, 053001 (2008).

[15] X. W. Cai, X. Wei, and C. M. Du, Thermal plasma treatment and co-processing of sludge for utilization of energy and material, Energy Fuels **34**, 7775 (2020).

[16] Y. Byun, W. Namkung, M. Cho, J. W. Chung, Y. S. Kim, J. H. Lee, C. R. Lee, and S. M. Hwang, Demonstration of thermal plasma gasification/vitrification for municipal solid waste treatment, Environ. Sci. Technol. **44**, 6680 (2010).

[17] M. Baeva, M. S. Benilov, N. A. Almeida, and D. Uhrlandt, Novel nonequilibrium modelling of a dc electric arc in argon, J. Phys. D **49**, 245205 (2016).

[18] H. X. Wang, T. Zhu, S. R. Sun, G. Liu, and A. B. Murphy, Chemical nonequilibrium modelling of a free-burning nitrogen arc, J. Phys. D **53**, 505205 (2020).

[19] P. Liang and J. P. Trelles, 3D numerical investigation of a free-burning argon arc with metal electrodes using a novel sheath coupling procedure, Plasma Sources Sci. Technol. **28**, 115012 (2019).

[20] W. X. Pan, Z. Y. Guo, X. Meng, H. J. Huang, and C. K. Wu, Fluctuation characteristics of arc voltage and jet flow in a nontransferred dc plasma generated at reduced pressure, Plasma Sources Sci. Technol. **18**, 045032 (2009).

[21] C. Wang, L. Sun, Q. Sun, Z. L. Zhang, W. L. Xia, and W. D. Xia, Experimental observations of constricted and diffuse anode attachment in a magnetically rotating arc at atmospheric pressure, Plasma Chem. Plasma Process. **39**, 407 (2019).

[22] K. Shao, Y. H. Hu, X. Meng, H. J. Huang, S. R. Sun, and H. X. Wang, Experimental study on the restrike mode of a dc arc anode attachment, Plasma Chem. Plasma Process. **41**, 1517 (2021).

[23] H. Guo, P. Li, H. P. Li, N. Ge, and C. Y. Bao, *In situ* measurement of the two-dimensional temperature field of a dual-jet direct-current arc plasma, Rev. Sci. Instrum. **87**, 053001 (2016).

[24] X. Xiao, X. M. Hua, F. Li, and Y. X. Wu, Spectroscopic measurement of temperature and gas composition in Ar-N$_2$ shielded TIG welding, Weld. World **60**, 1287 (2016).

[25] Y. H. Hu, X. Meng, H. J. Huang, A. B. Murphy, K. Shao, S. R. Sun, and H. X. Wang, A novel anode structure for diffuse arc anode attachment, J. Appl. Phys. **54**, 36LT01 (2021).

[26] O. H. Nestor, Heat intensity and current density distributions at the anode of high current, inert gas arcs, J. Appl. Phys. **33**, 1638 (1962).

[27] E. Pfender and J. V. R. Heberlein, Heat transfer processes and modeling of arc discharges, Adv. Heat. Trans. **40**, 345 (2007).

[28] J. V. R. Heberlein, J. Mentel, and E. Pfender, The anode region of electric arcs: A survey, J. Phys. D **43**, 023001 (2010).

[29] L. Wermer, J. K. Lefkowitz, T. Ombrello, M. S. Bak, and S. K. Im, Spatiotemporal evolution of the plasma from dual-pulsed laser-induced breakdown in an atmospheric air, Plasma Sources Sci. Technol. **27**, 015012 (2018).

[30] T. Hoder, D. Loffhagen, J. Voráč, M. M. Becker, and R. Brandenburg, Analysis of the electric field development and the relaxation of electron velocity distribution function for nanosecond breakdown in air, Plasma Sources Sci. Technol. **25**, 025017 (2016).

[31] S. Huang, T. Li, P. Ma, S. Y. Xie, Z. F. Zhang, and R. Chen, Quantitative evaluation of the breakdown process of spark discharge for spark-ignition engines, J. Phys. D **53**, 045501 (2020).

[32] E. Parkevich, G. Ivanenkov, M. Medvedev, A. I. Khirianova, A. S. Selyukov, A. V. Agafonov, A. R. Mingaleev, T. A. Shelkovenko, and S. A. Pikuz, Mechanisms responsible for the initiation of a fast breakdown in an atmospheric discharge, Plasma Sources Sci. Technol. **27**, 11LT01 (2018).

[33] M. S. Benilov, Understanding and modelling plasma-electrode interaction in high-pressure arc discharges: A review, J. Phys. D **41**, 144001 (2008).

[34] B. Jüttner, Cathode spots of electric arcs, J. Phys. D **34**, R103 (2001).

[35] H. P. Li and M. S. Benilov, Effect of a near-cathode sheath on heat transfer in high-pressure arc plasmas, J. Phys. D **40**, 2010 (2007).

[36] H. Barati, A. Kharicha, M. Al-Nasser, D. Kreuzer, G. Hackl, M. Gruber, A. Ishmurzin, C. Redl, I. O. Teplyakov, M. H. Wu, and A. Ludwig, MHD instability at the cathode spot as the origin of the vortex formation in high-intensity plasma arcs, J. Phys. Commun. **6**, 015008 (2022).

[37] D. F. Santos, M. Lisnyak, N. A. Almeida, L. G. Benilova, and M. S. Bennilov, Numerical investigation of AC arc ignition on cold electrodes in atmospheric-pressure argon, J. Phys. D **54**, 195202 (2021).

[38] L. H. Phan, S. Tashiro, H. V. Bui, T. Suga, T. Sato, and M. Tanaka, Investigating cathode spot behavior in argon alternating current tungsten inert gas welding of aluminum through experimental observation, J. Phys. D **52**, 26LT02 (2019).

[39] J. Schein, M. Schumann, D. Nandelstadt, and J. Mentel, Investigations of the ignition of arc spots on cold cathodes in a noble gas atmosphere, IEEE Trans. Plasma Sci. **25**, 897 (1997).

[40] J. A. Buendia and A. Venkattraman, Field enhancement factor dependence on electric field and implications on microscale gas breakdown: Theory and experimental interpretation, Europhys. Lett. **112**, 55002 (2015).

[41] J. H. Sun, S. R. Sun, C. Niu, and H. X. Wang, Non-equilibrium modeling on the plasma-electrode interaction in an argon dc plasma torch, J. Phys. D **54**, 465202 (2021).

[42] A. V. Keudell and V. S. Gathen, Foundations of low-temperature plasma physics: An introduction, Plasma Sources Sci. Technol. **26**, 113001 (2017).

[43] J. J. Lowke, A. B. Murphy, and M. Tanaka, Cathode spot formation possibly explained by cathode electron emission from impact of excited state atoms, J. Phys. D **52**, 444004 (2019).

[44] F. B. Dunning, A. C. H. Smith, and R. F. Stebbings, Secondary electron ejection from metal surfaces by metastable atoms. I. Measurement of secondary emission coefficients using a crossed beam method, J. Phys. B **4**, 1683 (1971).

[45] F. B. Dunning and A. C. H. Smith, Secondary electron ejection from metal surfaces by metastable atoms. II. Measurements of secondary emission coefficients using a gas cell method, J. Phys. B **4**, 1696 (1971).

[46] A. V. Phelps and Z. L. Petrovic, Cold-cathode discharges and breakdown in argon: Surface and gas phase production of secondary electrons, Plasma Sources Sci. Technol. **8**, R21 (1999).

[47] K. Shao, S. R. Sun, X. Meng, H. J. Hunag, Y. H. Hu, and H. X. Wang, Experimental study of the effect of argon on the restrike characteristics of nitrogen arc, Plasma Sources Sci. Technol. **31**, 095008 (2022).

[48] S. R. Sun, S. Kolev, H. X. Wang, and A. Bogaerts, Investigations of discharge and post-discharge in a gliding arc: A 3d computational study, Plasma Sources Sci. Technol. **26**, 055017 (2017).

[49] J. H. Sun, S. R. Sun, L. H. Zhang, and H. X. Wang, Two-temperature chemical nonequilibrium modeling of argon dc arc plasma torch, Plasma Chem. Plasma Process. **40**, 1383 (2020).